Journal of Materials Chemistry A

ROYAL SOCIETY OF CHEMISTRY

PAPER

View Article Online
View Journal | View Issue

Cite this: J. Mater. Chem. A, 2022, 10, 24746

Ultrahigh fluid sorption capacity of superhydrophobic and tough cryogels of cross-linked cellulose nanofibers, cellulose nanocrystals, and $Ti_3C_2T_x$ MXene nanosheets†

Golnoosh Akhlamadi, [ab] Elaheh K. Goharshadi*[acd] and Henrikki Liimatainen [*b]

In this study, we present superhydrophobic, hierarchical, and nanostructured cryogels made from a nanocellulose (NC) skeleton comprising cellulose nanofibers (CNFs) and nanocrystals (CNCs), double cross-linked with $Ti_3C_2T_x$ MXene nanosheets and poly(vinyl alcohol) (PVA) in the presence of tetradecylamine. Compared to pure CNCs or CNFs, cryogels with a combination of CNCs and CNFs possessed significantly better mechanical performance. Unlike many green natural based nanoporous solids, the prepared mixed cryogels displayed rigid and durable structure, and possessed ultrahigh sorption capacity for several organic fluids, among the highest reported for aerogels/cryogels in the literature. By taking advantage of the synergistic effects of crosslinking between long-entangled CNFs with short-needle-like CNCs as well as the strong interaction between NCs, MXene nanosheets and PVA, highly porous (>92%), lightweight (~20 mg cm^{-3}), and superhydrophobic cryogels with a water contact angle of ~150° were designed. The hybrid cryogels possessed ultrahigh sorption capacity toward various oils/organic solvents ranging from approximately 110–320 times their weight. The cryogels were reused in more than ten cycles of sorption–squeezing without significantly reducing sorption capacity. Hence, these nanostructured porous solids have a high potential to be used in various purposes in environmental remediation, such as oil spill response and removal of water-insoluble organic solvents.

Received 15th August 2022
Accepted 7th November 2022

DOI: 10.1039/d2ta06437e

rsc.li/materials-a

1. Introduction

With three dimensional (3D) interconnected network of nano- and micropores, aero- and cryogels, *i.e.*, lightweight porous solids constructed *via* supercritical or freeze–drying processes, are among the most promising designs for fluid sorbents because of their super-low density, large specific surface area, and porosity.[1–4] These materials have a high potential for use in environmental remediation, such as oil spill response and removal of water-insoluble organic solvent leakages and industrial oily wastewaters.[5–7] Generally, the materials used for oil or solvent removal possess superhydrophobicity and/or superoleophilicity to enable selective filtration or uptake of oil or solvent from aqueous mixtures,[8,9] or they promote water removal,[10] or controllable separation of different phases.[11] Several types of aerogels based on inorganics,[12,13] and synthetic[14–16] and natural polymers[17,18] have been revealed as superabsorbents. However, due to the mechanical brittleness of inorganic aerogels (*e.g.*, silica aerogels), their use and recovery in fluid separation are limited. Despite several favorable properties of carbon-based aerogels, the shortcomings such as expensive precursors and complicated or time-consuming fabrication processes hamper their use in practical applications.[6,19,20] By contrast, aero- and cryogels based on biopolymers can be created from abundant and cheap renewable biomass sources such as wood chips and agricultural residues, being highly appealing, sustainable, and biodegradable structures for removal of oil and organic solvents from aqueous environments.[10,21–24]

Recently porous solids derived from cellulose nanomaterials, such as cellulose nanofibers (CNFs) and nanocrystals (CNCs), have attracted considerable research interest.[25–27] In most studies, CNCs or CNFs are used as a single component for the preparation of nanocellulose (NC)-based aerogels,[28–30] while very few reports focus on mixing different sizes of NC to prepare aerogels. Zhang *et al.*[31] combined CNFs and CNCs from eucalyptus wood pulp. The mixed aerogel of CNCs and CNFs showed a better performance compared to pure CNCs or CNFs aerogels.

[a]Department of Chemistry, Faculty of Science, Ferdowsi University of Mashhad, Mashhad, 9177948974, Iran
[b]Fiber and Particle Engineering Research Unit, University of Oulu, PO Box 4300, FI-90014, Oulu, Finland
[c]Nano Research Center, Ferdowsi University of Mashhad, Mashhad, 9177948974, Iran
[d]Micro-Nano Technologies in Renewable Energies Center, Ferdowsi University of Mashhad, Mashhad, 9177948974, Iran. E-mail: Henrikki.Liimatainen@oulu.fi; gohari@um.ac.ir

† Electronic supplementary information (ESI) available. See DOI: https://doi.org/10.1039/d2ta06437e

Despite the many intriguing features attributed to biobased NC aero- and cryogels, major challenges still limit their harnessing as fluid sorbents. When NC materials are exposed to an aqueous environment, their inherent strong hydrophilicity causes the porous structure to collapse, decreasing the interaction between the sorbent and nonpolar compounds. To solve this problem, the NC surface has been modified with hydrophobic molecules such as organosilicates.[32–34] Furthermore, the porous NC materials' low mechanical integrity and flexibility have a negative impact on their use and shape recovery. To overcome this limitation, the NC network can be interlinked through covalent reactions and/or *via* hydrogen bond interactions.[35–39]

The new generation of 2D nanomaterials provides an alternative approach to enhancing the NC aerogel characteristics. For this purpose, MXenes nanosheets, which belong to a large family of transition metal carbides, nitrides, and carbonitrides, possess a unique layered structure and versatile interfacial chemistry.[40] MXenes, with a general chemical formula of $M_{n+1}X_nT_x$, are primarily synthesized by selectively etching the A-group (mainly group IIIA or IVA elements) layers from their precursor materials $M_{n+1}AX_n$ phases ($n = 1$, 2, or 3), where M is an early transition metal (V, Ti, Mo, Ta, *etc.*); A represents Al, Si, Ga, *etc.*; and X is C and/or N.[41,42] Titanium carbide ($Ti_3C_2T_x$), where T_x denotes the surface functional groups (–OH, –O, –F and/or –Cl) forming on the surface of the outer M elements during synthesis, is the most widely studied member of the MXene family in the context of water purification and environmental remediation because of its high surface area, hydrophilicity, surface functionality, abundance, facile scale-up synthesis, and environmentally benign characteristics.[43,44] Up to now, only few studies have been reported on the incorporation of MXene nanosheets in aero- and cryogels for fluid sorption.

An ultralight MXene aerogel with a density of <10 mg cm^{-3} and sorption capacity of 35–90 g g^{-1} for organic solvents and oils was prepared in a dry ice bath followed by vacuum drying.[45] Using freeze–drying and thermal imidization, a polyimide/MXene 3D aerogel was fabricated to obtain an oil sorption capacity of ~18–58 g g^{-1}.[40] An ultralow density (9.98 mg cm^{-3}) multifunctional conductive polyimide nanofiber/MXene composite aerogel with a sorption capacity of 56–135 g g^{-1} for various oil and organic solvents was fabricated.[46] A MXene-based melamine sponge (MS) was prepared by a simple dip-coating method.[47] Hydrogen bonding interaction between the amino groups on the skeleton of the MS and polar groups on the surface of the as-exfoliated 2D MXene $Ti_3C_2T_x$ nanosheets resulted in a hydrophobic sponge with a sorption capacity of 176 g g^{-1} for various oils. Wood-inspired aerogel was designed by dispersing CNCs and MXene nanosheets into a polyurethane matrix to form a functional network for oil/organic solvents separation with a sorption capacity of 45 to 63 g g^{-1} and WCA ≈ 152°.[48] Therefore, a combination of MXenes with synthetic materials can provide appealing characteristics for fluid sorption. This approach could potentially be used to create advanced porous hybrids of sustainable raw materials and MXenes. In addition, NC can also be combined with polymers such as poly(vinyl alcohol) to prepare a composite aerogel with improved mechanical properties.[33,49,50] PVA is a low-cost, water-soluble, biodegradable, and nontoxic polymer with good chemical stability and reactivity.[51]

To the best of our knowledge, cryogels created by mixing two types of NC materials and MXene nanosheets have not previously been revealed. In this study, we prepared superhydrophobic and mechanically tough cryogels of cellulose nanofibers and nanocrystals double cross-linked with $Ti_3C_2T_x$ MXene nanosheets and PVA. Benefiting from the strong interaction between NC, MXene nanosheets and PVA chains, ultralight, highly porous, and recyclable CNCs–CNFs/PVA/TDA@MXene cryogels with ultrahigh sorption capacity toward various oils and organic solvents were fabricated. MXene was synthesized by selectively etching of Ti_3AlC_2 precursors and was further mixed with CNCs, CNFs, tetradecylamine (TDA), and PVA to produce hybrid cryogels using freeze–drying.

2. Experimental section

2.1. Materials

Bleached softwood kraft pulp sheets were supplied from Metsä Fibre, Finland (dry matter content 94.7%). Choline chloride (ChCl, >98%), oxalic acid dihydrate, and urea (97%) were purchased from Algry Quimica SL (Spain), Sigma Aldrich (Germany), and Borealis (Austria), respectively. MAX phase (Ti_3AlC_2, 400 mesh) was obtained from Jilin 11 Technology Co., Ltd (China). Lithium fluoride (LiF, 99.995%), hydrochloric acid (HCl, 37%), poly(vinyl alcohol) (PVA, M_w 85 000–124 000), and tetradecylamine (TDA, 95%) were purchased from Sigma Aldrich (Germany). Silicon oil, linseed oil, chloroform (>99%), *n*-hexane (>98%), toluene (>99.9%), acetone (>99.8%), dimethylformamide (DMF, >99.9%), and methanol (>99.9%) were obtained from VWR Chemicals (Finland). Tetrahydrofuran (>99.5%, THF) was purchased from Merck (Germany). Gasoline (E95) and motor oil (5W40) were bought from a local gas station. All solutions were prepared with deionized (DI) water. All chemicals were used as received without further purification.

2.2. Fabrication of CNCs and CNFs

CNCs were prepared using the previously reported method based on acidic deep eutectic solvents (DES).[52] DES components (63.06 g of choline chloride and 56.94 g of oxalic acid dihydrate, molar ratio 1 : 1) were mixed in a beaker and put in an oil bath at 100 °C for 30 min. When a clear solution was obtained, 1.2 g of dried softwood pulp sheets were added into the DES in the form of small, torn pieces and mixed at 100 °C for 6 h. The reaction was then stopped by adding DI water. The DES-treated fibers were filtered and washed with DI water. For the liberation of nanocrystals from the treated fibers, fibrous cellulose pulp was diluted to a 0.5 wt% consistency, mixed with Ultra Turrax with 8000 rpm (IKA T25, Germany) for 2 min, and then converted into individual nanocrystals using a microfluidizer (Microfluidics M-110EH-30, USA). The suspension was passed three times through 400 and 200 μm at a pressure of 1300 bar. Afterward, the suspensions were passed three times through a combination of 400 and 86 μm chambers at the pressure of 1500 bar. The obtained CNCs suspension was clear and only

slightly viscous. A rotary vacuum device (Büchi Rotavapor R-114, Germany, connected with a water bath Büchi Waterbath B-480, Germany) was used to concentrate it to the necessary consistency. A detailed characterization of the CNCs obtained has been reported previously.[53]

CNFs were obtained using a combined pretreatment of DES of choline chloride–urea and mechanical disintegration with a microfluidizer.[54] A DES solution was prepared by melting 1620 g of choline chloride and 1223 g of urea (molar ratio 1 : 2) in a large beaker (5 L) in an oven at 100 °C for the pretreatment of cellulose pulp sheets. Then, it was placed into an oil bath at 100 °C under constant stirring for 15 min to obtain a clear liquid, and 25 g of ripped pulp sheets were added to the suspension and mixed for 2 h. After removing the beaker from the oil bath, DI water was added to the mixture to quench the reaction. Finally, the suspension was filtered and washed with DI water. The treated fibers were diluted to a consistency of 0.5 wt% and nanofibrillated using a microfluidizer. The sample was passed three times through 400 and 200 μm chambers at the pressure of 1000 bar, followed by two times through 400 and 100 μm chambers at the pressure of 1300 bar. A detailed characterization of the prepared CNFs has been reported previously.[54]

2.3. Synthesis of $Ti_3C_2T_x$ MXene nanosheets

$Ti_3C_2T_x$ MXene nanosheets were prepared by the selective etching of Al layers/elements of Ti_3AlC_2 MAX phase powder using LiF and HCl, followed by exfoliation.[55] At first, the etching mixture was prepared by adding 0.8 g (0.031 mol) of LiF to 10 ml of 9 M HCl solution in a 50 ml Teflon beaker. The mixture was stirred at room temperature for 15 min until all LiF powder was dissolved into the HCl solution. Subsequently, 0.5 g (0.0025 mol) of Ti_3AlC_2 powder was gradually added in small portions for 15 min to the etching solution in an ice bath to avoid overheating. The etching reaction continued at 35 °C under continuous magnetic stirring for 24 h to remove the Al layer. Afterward, the acidic etched powders were washed several times with DI water *via* centrifugation (5 min for each cycle at 3500 rpm) until the supernatant reached a pH of about 6. The sediments were dispersed in 120 ml degassed DI water and were then sonicated (250 W, 50% amplitude, and cycle 0.8) with constant stirring in an ice bath for 1 h to delaminate the multilayer $Ti_3C_2T_x$ into single layers. The ultrasonication process was performed under Ar flow to prevent the MXene oxidation. Finally, the resulting solution was centrifuged at 3500 rpm for 1 h, to separate the single-layer nanosheets from the multilayer MXene and unexfoliated MAX phase, and the dark green supernatant was collected as MXene suspension (0.5 mg ml^{-1}, 3 mM).

2.4. Preparation of reference and CNCs–CNFs@MXene cryogels with different composition

First, reference cryogels were fabricated only from nanocellulose using aqueous CNCs and CNFs suspensions with different mass ratios (1 : 1, 1 : 2, 1 : 3, 1 : 4, 2 : 1, 3 : 1, and 4 : 1) and concentrations (0.3, 0.6, and 1 wt%). The suspensions were mixed with Ultra Turrax for 2 min at 8000 rpm, and then stirred at 500 rpm for 24 h. To produce the CNCs–CNFs cryogels, the uniform NC suspensions were poured into the Teflon molds, placed in liquid nitrogen, and freeze-dried for 72 h at −54 °C using a Scanvac Coolsafe freeze-dryer (55–15 Pro, Denmark) with a vacuum pressure of ∼0.01 mbar. The sample with a CNCs : CNFs 3 : 1 ratio and 1 wt% showed the best mechanical strength without any visible cracks in its structure and was chosen for further tests.

Hydrophobized, mixed nanocellulose cryogels were synthesized using different amounts of TDA (0.1, 0.5, 0.8, 1.0, and 1.5 mg), which were dissolved in ethanol and sonicated for 2 min, added dropwise into CNCs–CNFs suspensions (20 ml, 3 : 1, 1 wt%, prepared as described in the previous section), and stirred for 30 min. Then, all suspensions were frozen in a liquid nitrogen bath and dried in a freeze–dryer. Finally, the obtained cryogels were placed in an oven at 80 °C for 16 h to complete the reaction. The cryogel possessing 0.8 mg TDA had the highest contact angle and was selected for further studies.

CNCs–CNFs/TDA@MXene cryogels with different mass ratios (1 : 3, 1 : 5, and 1 : 10) and concentrations (0.1, 0.3, 0.5, 0.8, and 1 wt%) of MXene to CNCs–CNFs solution were prepared using a constant NC concentration (CNCs to CNFs = 3 : 1, 1 wt%) and TDA amount (0.8 mg/20 ml). MXene suspension was added dropwise into the nanocellulose solution and stirred at 500 rpm for 2 h. After adding TDA and stirring the solution for 30 min, it was frozen in a liquid nitrogen bath, freeze-dried, and finally, the obtained cryogels were placed in an oven at 80 °C for 16 h. The cryogel with the MXene to NC ratio of 1 : 10 containing 0.5 wt% MXene solution resulted in the most uniform structure and was used for further tests.

CNCs–CNFs/PVA/TDA@MXene cryogels were fabricated using different ratios of PVA to CNCs–CNFs (1 : 1, 1 : 2, 1 : 3, and 1 : 4) and PVA concentrations (1, 2, 3, 4, and 5 wt%). At first, PVA and NC solution was mixed for 3 h at 500 rpm. Then, MXene was added dropwise and mixed for another 2 h, followed by mixing with TDA for 30 min. Finally, the solution was placed in a liquid nitrogen and freeze-dried. The best cryogel structure, CPMT cryogel, was obtained with the PVA ratio of 1 : 3 with 4 wt% and used for oil/water separations.

2.5. Characterizations

The powder X-ray diffraction (XRD) patterns of Ti_3AlC_2 MAX phase and $Ti_3C_2T_x$ MXene nanosheets were determined using a Rigaku SmartLab 4.5 kW XRD instrument (Japan) in a continuous scan mode with a five-axis θ-θ goniometer, with the Co source (40 kV and 135 mA) Kα (Kα1 = 1.78892 Å; Kα2 = 1.79278 Å; Kα1/Kα2 = 0.5) at the scan rate of 4°min^{-1} and step width of 0.02° from a 2θ angle of 5°–130°. The d-spacing of MAX phase and MXene nanosheets were calculated using Bragg's law:

$$n\lambda = d \sin\theta \quad (1)$$

where n is an integer (1, 2, 3, …), λ is the X-ray wavelength, θ is the incident angle, and d is the spacing between diffraction

planes.[56] The crystallite size of materials was calculated using the Debye–Scherrer formula:

$$D = \frac{0.9\ \lambda}{\beta \cos \theta} \quad (2)$$

where β is the full width at half maximum (FWHM) of the dominating peak corresponding to the (002) plane.[57] Fourier transform infrared spectroscopy (FTIR) was used to determine the functional groups of the synthesized MXene powder at room temperature with a KBr pellet on a Thermo Nicolet-Avatar 370 FT-IR Spectrometer ranging from 400 to 4000 cm^{-1} (Thermo Nicolet, USA). The morphology of MAX phase, MXene, and cryogels was investigated using a field emission scanning electron microscope (FE-SEM) on a Zeiss Sigma instrument (Germany) with a 5 kV accelerating voltage combined with energy dispersive X-ray (EDX) spectroscopy for elemental mapping. Samples were analyzed by placing them on a sample holder using a carbon pad and coating it with a thin layer of platinum. Transmission electron microscopy (TEM) images of samples were obtained using JEOL JEM-2200FS EFTEM/STEM (Japan). The composition and the electronic states of the delaminated MXene were investigated using X-ray photoelectron spectroscopy (XPS) with Al-Kα using Thermo Fisher Scientific ESCALAB 250Xi XPS System (USA). CasaXPS and Origin software with a Shirley background type were used for the XPS peak fitting. The atomic force microscopy (AFM) images of prepared MXene nanosheets were obtained by Ara Research (model no. 0101/A, Iran) in a noncontact mode at room temperature. A Zetasizer (Nano-ZS) (Malvern, United Kingdom) was used to measure zeta potential. The surface wettability of cryogels was determined using the sessile drop technique using Krüss DSA 25 (Krüss GmbH, Hamburg, Germany) by placing a 4 μL drop of DI water on the cryogel surface and capturing CCD images at the rate of 1 frame per s. The contact angle was determined based on the drop's shape analysis using the full Young–Laplace equation and assuming a spherical drop.

2.6. Density and porosity of cryogels

The mass and volume of the cryogels were used to calculate their density. The mass of the cryogels was measured by an analytical balance (readability 0.0001 g), and the volume was calculated by measuring diameters and heights with a digital caliper at three different positions.

The NC cryogels porosity (P%) was calculated according to the following equation:

$$P\ (\%) = \left(1 - \frac{\rho_{\text{aerogel}}}{\rho_s}\right) \times 100\% \quad (3)$$

where ρ_{cryogel} and ρ_s are the density of the bulk cryogel samples and solid materials, respectively. The solid density, r_s, was calculated using the following equation:

$$\rho_s = \frac{1}{\frac{m_{\text{cellulose}}}{\rho_{\text{cellulose}}} + \frac{m_{\text{PVA}}}{\rho_{\text{PVA}}} + \frac{m_{\text{Ti}_3\text{C}_2\text{T}_x}}{\rho_{\text{Ti}_3\text{C}_2\text{T}_x}} + \frac{m_{\text{TDA}}}{\rho_{\text{TDA}}}} \quad (4)$$

where $m_{\text{cellulose}}$, m_{PVA}, m_{Ti3C2Tx}, and m_{TAD} are the mass fractions of cellulose, PVA, $Ti_3C_2T_x$, and TDA. $\rho_{\text{cellulose}}$, ρ_{PVA}, ρ_{Ti3C2T_x}, and ρ_{TAD} are the solid densities of cellulose (1.528 g cm^{-3}), PVA (1.29 g cm^{-3}), $Ti_3C_2T_x$ (4.91 g cm^{-3}),[58] and TDA (0.993 g cm^{-3}), respectively.

2.7. Solvents sorption capacity and recyclability of cryogels

Five oils, including gasoline, motor oil, silicon oil, cooking oil, and linseed oil, and seven organic solvents, *i.e.*, chloroform, *n*-hexane, acetone, methanol, toluene, DMF, and THF, were used to measure the sorption capacity of cryogels. Preweighted cryogels were immersed in oil/organic solvents for 3 min to reach sorption equilibrium. The swollen cryogels were then removed and weighed. The sorption capacity (Q, g g^{-1}) was calculated according to eqn (5):

$$Q = \frac{m_1 - m_0}{m_0} \quad (5)$$

where m_0 and m_1 are the mass of the cryogel before and after oil/organic solvent sorption, respectively. All tests were repeated in triplicate and made at room temperature. A cyclic compression test was performed to evaluate the recyclability of cryogels by simply squeezing the cryogels manually. For this purpose, two parallel glass slides were used to compress the soaked cryogels to remove the adsorbed oils or organic solvents. The sorption and squeezing processes were performed in 10 cycles using edible oil, motor oil, chloroform, and methanol as the model oils/organic solvents.

3. Results and discussion

3.1. Exfoliation of mxene nanosheets

Scheme 1 shows the synthesis of delaminated MXene nanosheets by selectively etching Al layers of Ti_3AlC_2 precursor *via* an *in situ*-produced HF (mixture of LiF/HCl). The extensive sonication led to the delamination of multilayered-$Ti_3C_2T_x$ terminated by fluorine, oxygen, and hydroxyl groups. A series of characterizations were conducted to verify the $Ti_3C_2T_x$ MXene nanosheets' successful preparation.

Fig. 1a shows the XRD patterns of the Ti_3AlC_2 MAX phase and $Ti_3C_2T_x$ MXene nanosheets. The crystallinity and structural order of Ti_3AlC_2 decrease after the etching treatment, confirming the removal of Al layers from Ti_3AlC_2 and the presence of the $Ti_3C_2T_x$ phase. The strong characteristic peaks

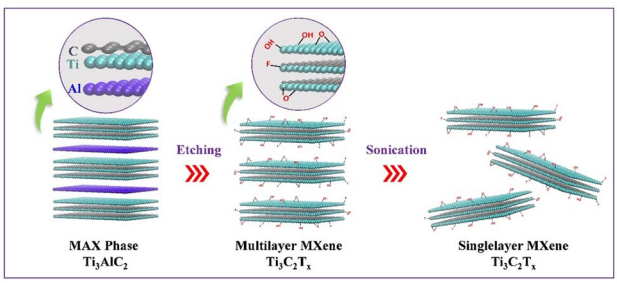

Scheme 1 Preparation of MXene nanosheets.

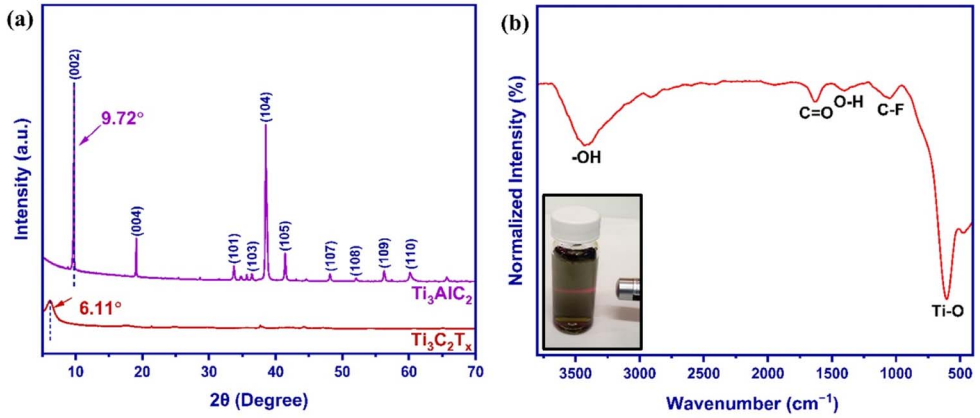

Fig. 1 (a) XRD patterns of Ti_3AlC_2 and $Ti_3C_2T_x$. (b) FTIR spectrum of $Ti_3C_2T_x$. Inset in (b) shows the Tyndall effect of $Ti_3C_2T_x$ dispersion.

of Ti_3AlC_2 at 9.72°, 19.10°, 33.76°, 36.44°, 38.49°, and 41.42° are assigned to the (002), (004), (101), (104), (104), and (105) crystal planes, respectively.[46,47,59] The most intense pyramidal plane peak (104) disappeared in the case of MXene compared with the Ti_3AlC_2 MAX precursor, indicating the successful elimination of Al atomic layers from Ti_3AlC_2 after the etching process.[46,60] Moreover, the MXene powder (002) basal plane peak significantly shifted to the lower 2θ angle (from 9.72° to 6.11°). It broadened, suggesting the increase of d-spacing from 10.56 to 16.79 Å due to the selective removal of Al atoms in Ti_3AlC_2 according to Bragg's law (eqn (1)).[47,56] Furthermore, the average crystallite size of Ti_3AlC_2 MAX phase and $Ti_3C_2T_x$

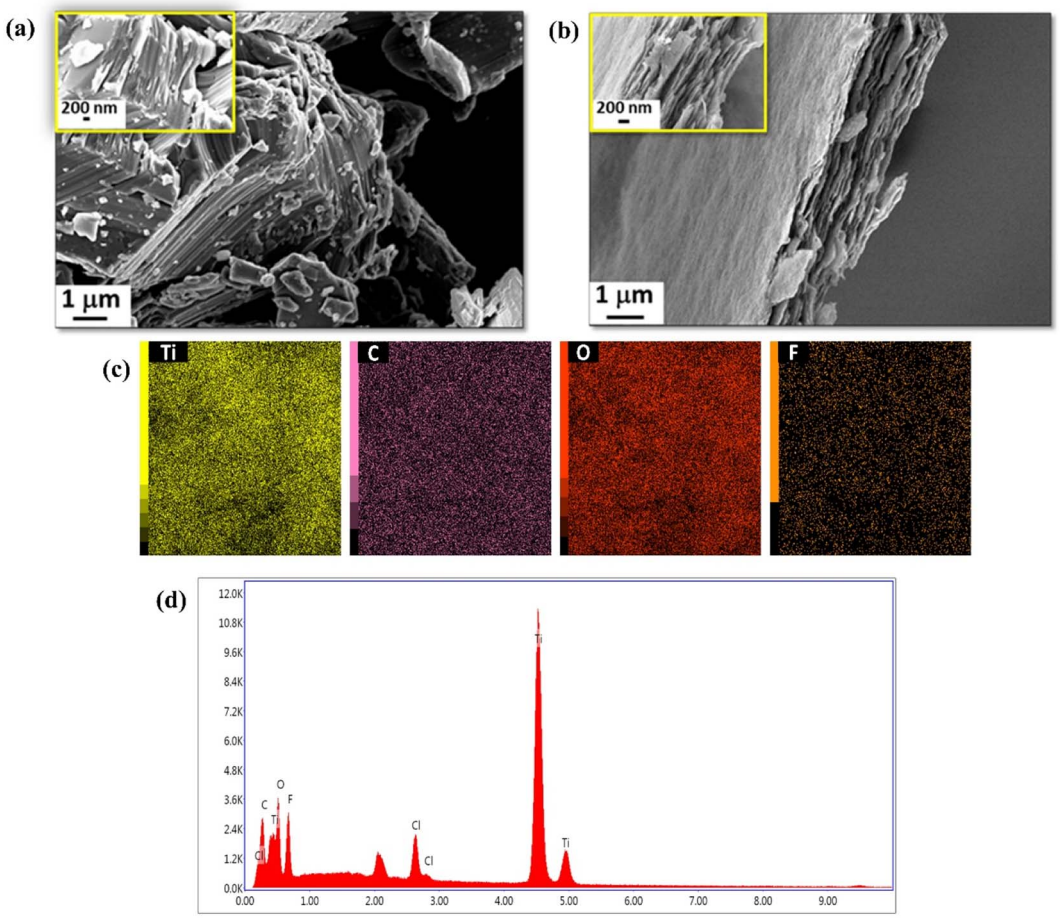

Fig. 2 Morphology structure of (a) MAX phase and (b) MXene. (c) Elemental mapping image and (d) EDX spectrum of MXene.

MXene reduced from 2.78 μm to 1.9 nm after etching (eqn (2)). These changes indicated that the Al layer was etched, and the MAX phase was converted successfully to delaminated MXene nanosheets.

FTIR spectroscopy (Fig. 1b) was used to determine the surface functional groups of MXene nanosheets. The bands at 3435 and 1400 cm^{-1} confirm the presence of the terminal hydroxyl groups and possibly absorbed H_2O molecules or extremely strongly coordinated H_2O. The bands at 1631, 1052, and 610 cm^{-1} are assigned to the stretching vibrations of C=O, C–F, and the deformation vibration of Ti–O bonds, respectively, which is consistent with previous reports.[60–62] The terminated functional groups (O, OH, and F) endow the exfoliated MXene nanosheets to form a stable colloidal suspension in water. The dark green aqueous MXene nanosheet dispersion (with a Cs% = 0.5) exhibits a special "Tyndall effect," indicating the excellent stability and nanosize of MXene nanosheets and evidence for fabricating high-quality MXene nanosheets (inset of Fig. 1b).[55] Furthermore, due to the hydrophilic functional groups on the surface of the prepared MXene nanosheets, the zeta potential was measured to be −32.27 mV.

FE-SEM images of MAX phase and MXene nanosheets were obtained to evaluate the etching process and analyze the morphology of nanosheets. The commercially purchased MAX phase powder shows a lamellar and close-packed structure composed of metallic and strong covalent/ionic bonds (Fig. 2a). Clearly, after etching and the delamination process, a loosely stacked accordion-like layered structure and an opened interspace of $Ti_3C_2T_x$ MXene nanosheets can be observed (Fig. 2b), confirming the successful etching of Ti_3AlC_2 and removal of Al layers. Also, the removal of aluminum was verified using EDX. The elemental mapping (Fig. 2c) and EDX spectrum (Fig. 2d) of MXene powder show that the exfoliated MXene mainly contains Ti (44.36 wt%), C (16.03 wt%), O (21.70 wt%), F (14.96 wt%), confirming the typical $Ti_3C_2T_x$ composition.[63–66] Only a negligible Cl amount (2.94 wt%) was observed as an impurity due to the use of HCl in the etching process, suggesting the high purity of prepared $Ti_3C_2T_x$ nanosheets.

As shown in TEM analysis (Fig. 3a), the MXene nanosheets possessed an ultralow thickness. The lateral diameter of MXene nanoflakes ranged from ~100 to 500 nm, with the average thickness of around 1 nm, as validated by an AFM image (Fig. 3c), corresponding to the single or double-layer structure of $Ti_3C_2T_x$ MXene.[67] The selected area electron diffraction (SAED) pattern in Fig. 3b shows the single-crystalline hexagonal structure of the nanosheets with a lattice spacing of 2.76 and 1.55 Å corresponding to the $Ti_3C_2T_x$ (100) and (−2 1 0). According to the MXene nanoflakes particle size distribution (PSD) (Fig. 3d), the mean volumetric diameter of nanosheets was about 23.75 nm.

XPS analysis was performed to investigate further the surface chemical composition and molecular structure of the as-prepared MXene (Fig. 4). The XPS survey spectra (Fig. 4a) show the typical peaks of Ti 2p, C1s, O1s, and F1s from 0 to 1300 eV, which suggest the presence of $Ti_3C_2T_x$ together with =O, –OH, –F groups as a result of HCl and LiF aqueous solution. The peaks with binding energy values of 35, 284, 456, 477, 531,

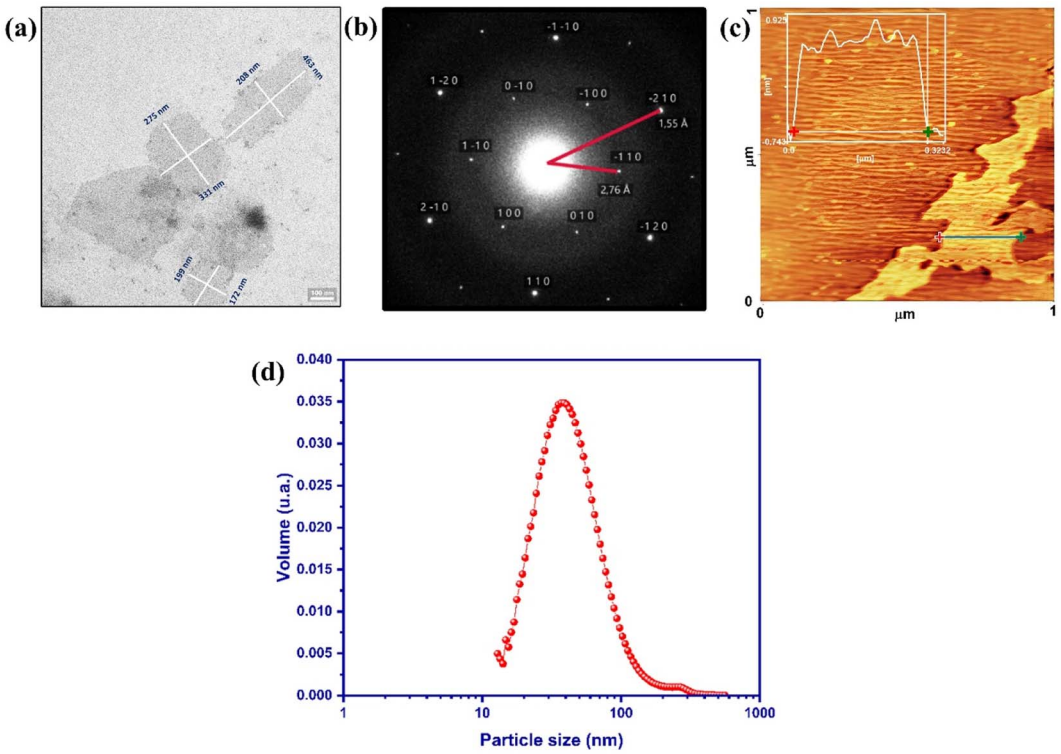

Fig. 3 (a) TEM image, (b) its corresponding SAED pattern, (c) AFM image, and (d) PSD of MXene nanosheets.

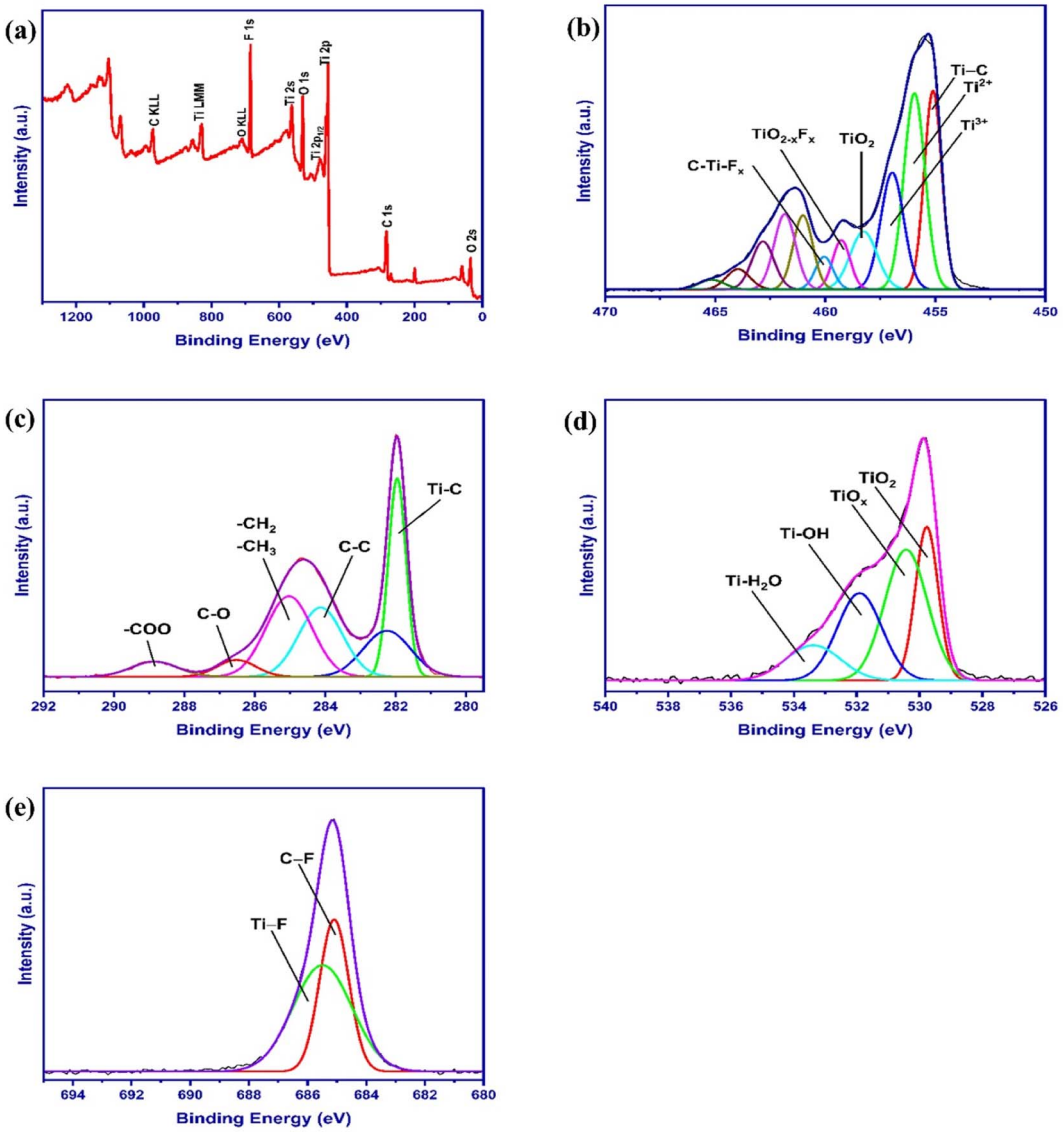

Fig. 4 (a) XPS survey spectrum of MXene and deconvolution of high-resolution XPS spectra for the elements in delaminated MXene nanosheets for (b) Ti 2p, (c) C 1s, (d) O 1s, and (e) F 1s.

562, 685, 830, and 978 eV are assigned to O 2s, C1s, Ti 2p, Ti $2p_{1/2}$, O1s, Ti 2s, F1s, Ti LMM, and C KLL,[68,69] respectively, which is consistent with the EDX results shown in Fig. 2d. Notably, it can be seen that the Al 2p peak does not exist in the spectra, which proves the fact that Al atoms are successfully etched from the Ti_3AlC_2 MAX phase. Fig. 4b–e show the deconvoluted spectra of Ti 2p, C 1s, O 1s, and F 1s within MXene powder. Table 1 summarizes the peak positions obtained from the fits. The Ti 2p core level peak can be fitted by a contribution of six doublets (Ti $2p_{3/2}$–Ti $2p_{1/2}$) corresponding to Ti atoms, Ti–O, TiO_2–xFx, and C–Ti–Fx. The C 1s region spectra of layered Ti_3C_2 are fitted by six peaks assigned to Ti–C,1, 2 hydrocarbons (–CH_2– & CH_3–), and carboxylates (–COO). The XPS spectra of O 1s are divided into O–Ti, C–Ti–O_x, C–Ti–$(OH)_x$, and H_2O–Ti bonds. The F 1s peak is deconvoluted into Ti–F and C–F bonds. The calculated binding energy values of the components are consistent with those obtained in previous XPS studies on $Ti_3C_2T_x$.[70–75] In summary, XPS analysis shows that MXenes nanosheets contain three types of surface functional groups: oxide (–O–), hydroxyl (–OH), and fluoride (–F), proving that etching treatment can introduce abundant hydrophilic surface termination O–H groups, which take part in covalent crosslinking and hydrogen bond interaction.

3.2. Characteristics of CNCs–CNFs@MXene cryogels

Fig. 5 shows a schematic representation of the general synthesis procedure and formation mechanism of the NC-MXene cryogels. In this work, cellulose nanomaterials, such as CNCs and CNFs, were produced using green DES-based pretreatments combined with microfluidization, and hybrid cryogels with different ratios and concentrations of CNCs

Table 1 $Ti_3C_2T_x$ XPS peak fitting results

Region	BE (eV)	FWHM (eV)	Assignment
Ti $2p_{3/2}$ ($2p_{1/2}$)	455.10 (461.01)	0.93 (1.03)	Ti (I, II or IV)
	455.94 (461.83)	1.12 (1.13)	Ti^{2+} (I, II, or IV)
	456.95 (462.82)	1.22 (1.18)	Ti^{3+} (I, II, or IV)
	458.25 (463.96)	1.43 (1.23)	TiO_2
	459.26 (465.15)	0.93 (1.33)	$TiO_{2-x}F_x$
	460.04 (465.99)	0.94 (1.03)	C–Ti–Fx (III)
C 1s	281.95	0.58	C–Ti–T_x
	282.24	1.57	C–Ti–T_x
	284.12	1.47	C–C
	285.02	1.54	$-CH_2-$ and $-CH_3$
	286.51	1.31	C–O
	288.85	1.54	–COO
O 1s	529.77	0.85	TiO_2
	530.42	1.59	C–T–O/TiO_2–F
	531.90	1.66	C–Ti–$(OH)_x$
	533.38	2.03	Ti–H_2O (adsorbed water)
F 1s	685.09	1.17	C–Ti–F_x (III)
	685.49	2.36	TiO_2–F

and CNFs were prepared. When the mixing ratio of CNCs and CNFs was 3 : 1 (solids content of 1 wt%), the Ref. cryogel presented good mechanical strength with no obvious cracks and high porosity of 99.61% compared to pure CNCs and CNFs aerogels. The excellent mechanical performance of Ref cryogel can be explained by a higher degree of crosslinking between long-entangled fiber-like CNFs and short-needle-like CNCs. Nevertheless, the hydrophilic character of the cellulose skeleton led to the collapse of the NC cryogels porous structure in the presence of water, limiting their use in oil/water separation. Therefore, TDA was used as a hydrophobization agent to improve the wet strength of the mixed NC cryogels.

Table 2 WCA of mixed CNCs–CNFs cryogels as a function of TDA dosage

CNCs–CNFs	TDA (mg)	WCA [°]
3 : 1, 1%	0.1	56.00
	0.5	62.40
	0.8	91.30
	1.0	84.09
	1.5	—

Table 2 shows the WCA of hydrophobized cryogels as a function of TDA dosage. By increasing the amount of TDA from 0.1 to 0.8 mg, the WCA of the cryogels increased from 56.00 to 91.30°, whereas it decreased at TDA contents greater than 0.8 mg. Moreover, the mixed cryogels with TDA content higher than 1 mg were very weak and disintegrated into powder after freeze–drying, and the WCA could not be measured. Also, the cryogels containing an optimized dosage of TDA (0.8 mg) suffered from poor mechanical performance, were easily collapsed or redisperse/disintegrated in water and had limited

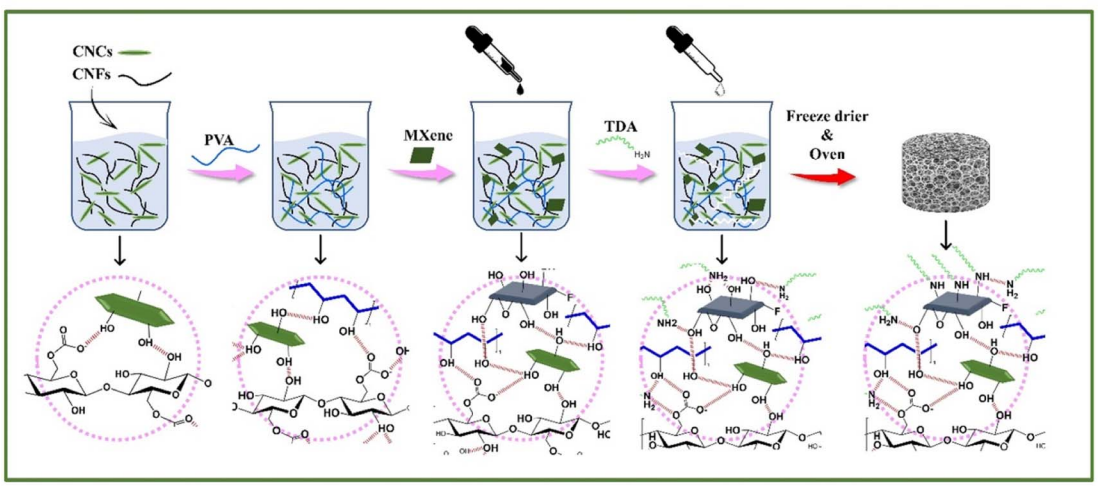

Fig. 5 Preparation of superhydrophobic and cross-linked CPMT cryogel containing MXenes.

shape recovery. Although they did not show any visible crack, the cryogels were very brittle when subjected to a slight compression.

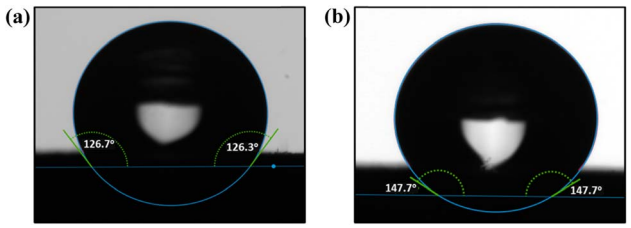

Fig. 6 WCA of (a) CMT and (b) CPMT cryogels.

The MXenes were incorporated into the cryogel structure to enhance the mechanical strength, hydrophobicity, and cross-linking of NC cryogels. As shown in Fig. 6a, the obtained NC cryogels containing MXenes and TDA (CMT) were strongly hydrophobic with a WCA of 126.7° and possessed a high porosity of 94.20%. Therefore, MXene nanoflakes acted as efficient cross-linkers in the CNCs/CNFs network and improved both the WCA and mechanical performance of cryogels. The presence of abundant hydroxyl groups on the surface of NC and MXene nanosheets promoted hydrogen bonding between the nano-constituents, while the amino groups of TDA reacted with surface hydroxyls during the heating process and reduced the surface free energy of cryogels.

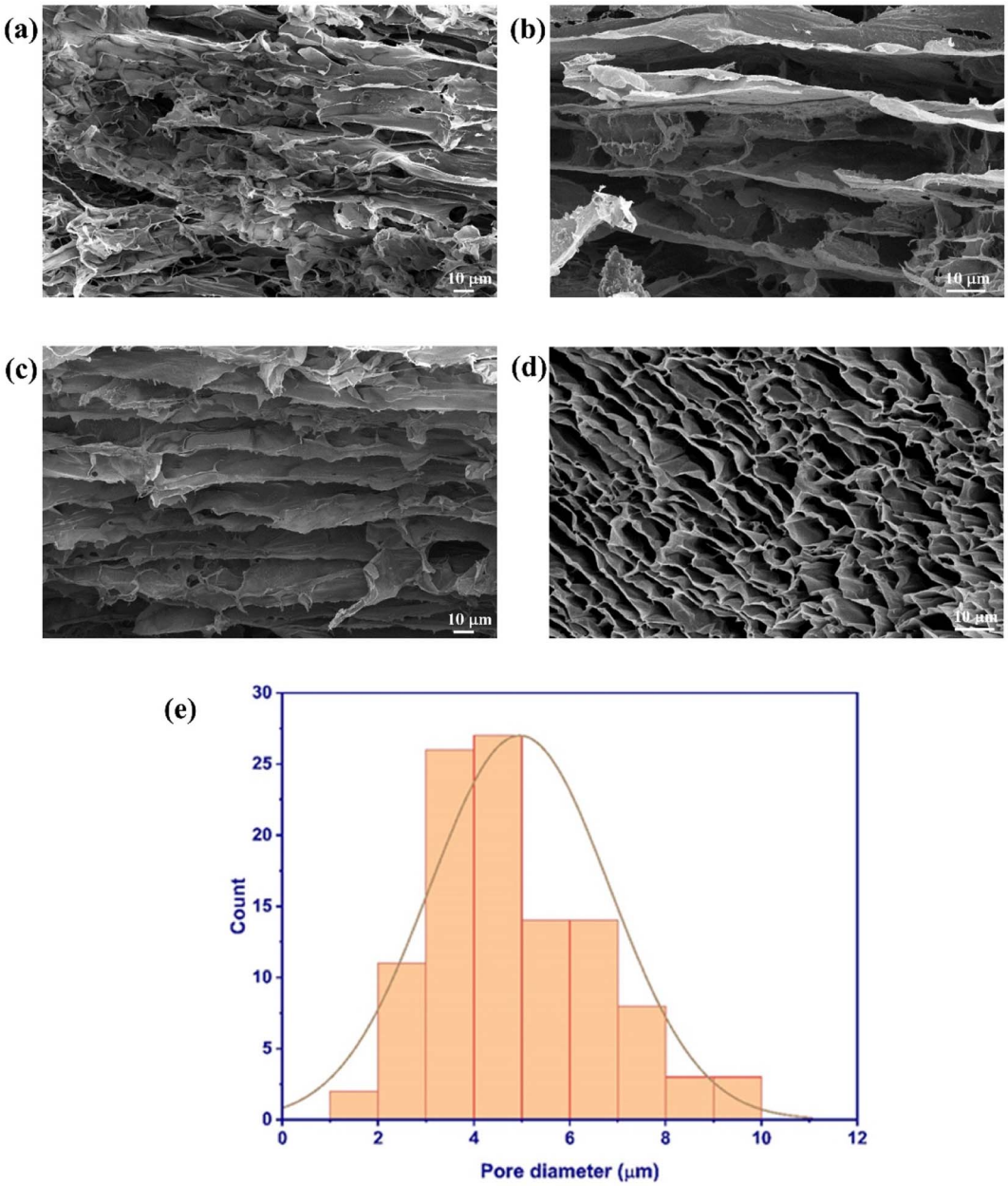

Fig. 7 FE-SEM of longitudinal structure of (a) Ref., (b) CMT, (c) CPMT cryogels; (d) cross-section of CPMT cryogel, and (e) average pore diameter of the CPMT cryogel.

PVA was introduced into the NC/MXene solution to further enhance cryogels (CPMT) durability *via* hydrogen bonding interactions between the hydroxyls of the PVA chains and the NC/MXene nanosheets.[76] PVA also enabled a more uniform MXene dispersion in the cryogel structure and provided more active sites for TDA, resulting in superhydrophobicity (WCA of 147.7°) (Fig. 6b).

Fig. 7 shows the morphology of Ref., CMT, and CPMT cryogels. The Ref. cryogel consisted of an irregular structure with closed pores and low porosity (Fig. 7a). This structure shows considerable shrinkage and pore collapse of the NC network due to capillary pressure during the freeze–drying. In contrast, MXene-containing cryogels (CMT and CPMT) showed a layered hierarchical structure that was open and very porous. These architectures are composed of lamellar, micrometer-sized macropores interconnected *via* CNCs–CNFs sheets in the longitudinal direction. FE-SEM images were used to study the pore structure of cryogels and to estimate the pore diameter using the open-source software ImageJ. Fig. 7d shows that the prepared CPMT cryogels have a complex, hierarchical, and interconnected 3D porous network structure with the average pore size distribution between 2 μm to 8 μm (Fig. 7e). The prepared interconnected channels formed a strongly cross-linked network with a stable pore structure and mechanical robustness. The aligned porous structure provides microchannels for liquid uptake and storage, which is beneficial for fluid sorption. These structural features were likely attributed to physical cross-linking between the MXenes nanosheets, NC, and PVA (hydrogen bonding and van-der-Waals interactions).

The compressive strength of Ref. and CPMT cryogels was illustrated using 200 g weights on the cryogels surface (Fig. 8). Due to the fragility of Ref. cryogel, a large compression was noticed when the material was loaded, and the structure was poorly recovered to its original shape after removing the weight, and a large deformation was observed. In contrast, the cross-linked porous network of NCs and MXenes nanoflakes can easily support a 200 g weight on the top of CPMT cryogel, showing only a very small compression. The CPMT also had a very low density of ~20 mg cm^{-3} and can stand on the flower petal, as shown in the inset of Fig. 8b. These results showed that the CPMT cryogel possessed both excellent mechanical strength and lightweight.

3.3. Sorption capacity, reusability, and chemical stability of CNCs–CNFs@MXene cryogels

The fluid sorption capacity of superhydrophobic/superoleophilic CPMT cryogels with a 3D porous network

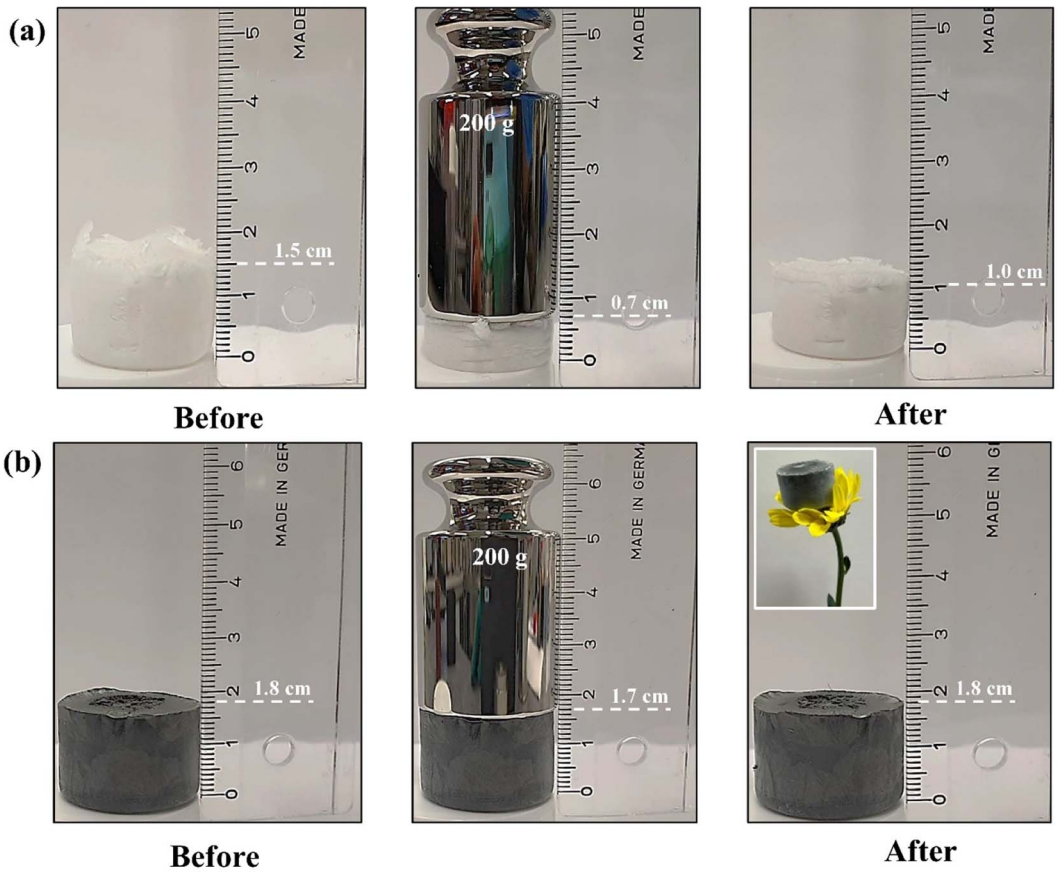

Fig. 8 (a) Ref. and (b) MXene containing CPMT cryogels before and after loading with a 200 g weight. Inset in d is CPMT cryogel standing on top of a flower.

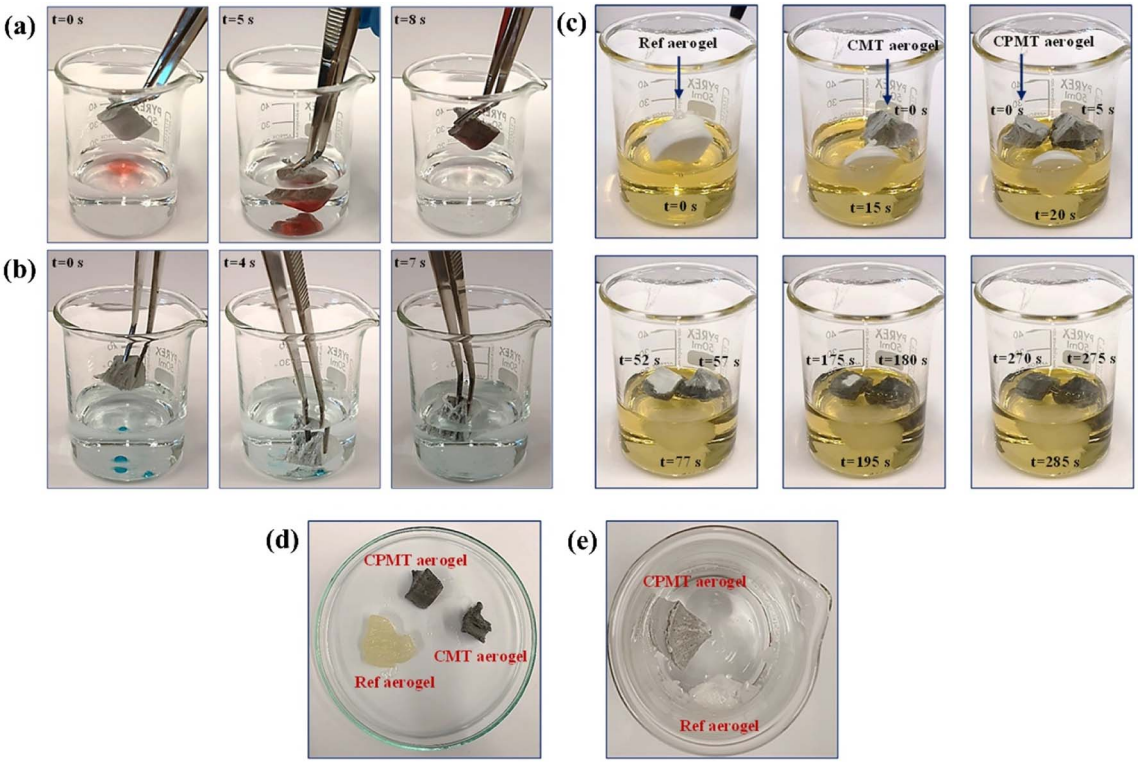

Fig. 9 Removal of (a) motor oil (dyed with oil red O) and (b) chloroform (dyed with methylene blue) from the surface and bottom of the water with CPMT cryogel, (c) the sorption performance of Ref., CMT, and CPMT cryogels as a function of time, (d) Ref., CMT, and CPMT cryogels after 1, 4, and 10 cycles of the edible oil sorption, and (e) Ref. and CPMT cryogels on the surface of the water.

structure was elucidated with several oils and organic solvents from water. When the cryogel was placed into the motor oil (stained with oil red O)/water mixture), it absorbed the floating oil on the water surface completely and quickly (<8 s), leaving the clean water, as shown in Fig. 9a (and Video S1†). Furthermore, the CPMT cryogel could selectively and quickly (<6 s) absorb organic solvents with a density greater than water, such as chloroform (dyed with methylene blue) underwater and was easily removed without any solvent release within 6 s (Fig. 9b, Video S2†). After sorption, the cryogel retained its shape and floated on the water surface without oil/solvent release, enabling easy sorbent collection in practical applications. Hence, the prepared cryogel is an ideal sorbent for treating oil spills and oily wastewater remediation.

Fig. 9c shows the sorption performance of Ref., CMT, and CPMT cryogels in edible oil. The Ref. cryogel was sinking in oil after approximately 1 min. By contrast, the modified CMT and CPMT cryogels were saturated with oil after approximately 3 and 5 min, respectively, but were still partly floating. The structure of Ref. cryogel collapsed when exposed to oil, and it was not possible to use it for the recycling test (Fig. 9d). The CMT and CPMT cryogels maintained their porous appearance and after four cycles of sorption–desorption of edible oil, the CMT cryogel structure failed to maintain its original shape. In comparison, the CPMT cryogel maintained its shape still after ten cycles without any obvious failure in its structure with super high oil sorption efficiency, as shown in Fig. 9d. The CPMT cryogel also had good wet strength, as shown when exposed to pure water, whereas Ref. cryogel lost its structural integrity after contact with water (Fig. 9e).

Seven organic solvents (chloroform, *n*-hexane, methanol, toluene, acetone, DMF, and THF) and five oils (gasoline, motor oil, silicon oil, edible oil, and linseed oil) were investigated to quantify the sorption efficiency of Ref., CMT, and CPMT cryogels (Fig. 10a). These substances are contaminants commonly existing in our daily lives and industries. The pristine NC cryogel (Ref.) had a sorption capacity ranging from 10 to 72 g g^{-1}, at a similar level to previously reported NC aerogels.[21] The introduction of MXene into the cryogel structure resulted in outstanding increase in sorption efficiency, with the sorption capacities of 107–278 g g^{-1}. Although this improvement was achieved without PVA, the shape recovery and recyclability of CMT cryogels were insufficient. Thus, PVA was incorporated in the mixture of CNCs/CNFs and MXenes, resulting in mechanically robust designs with a greater sorption capacity of 110–320 g g^{-1}. This excellent oil/organic solvent sorption performance was presumably assigned to superhydrophobicity and the channeled and hierarchical microporous structure of CPMT, which promoted the capillary uptake of nonpolar fluids.

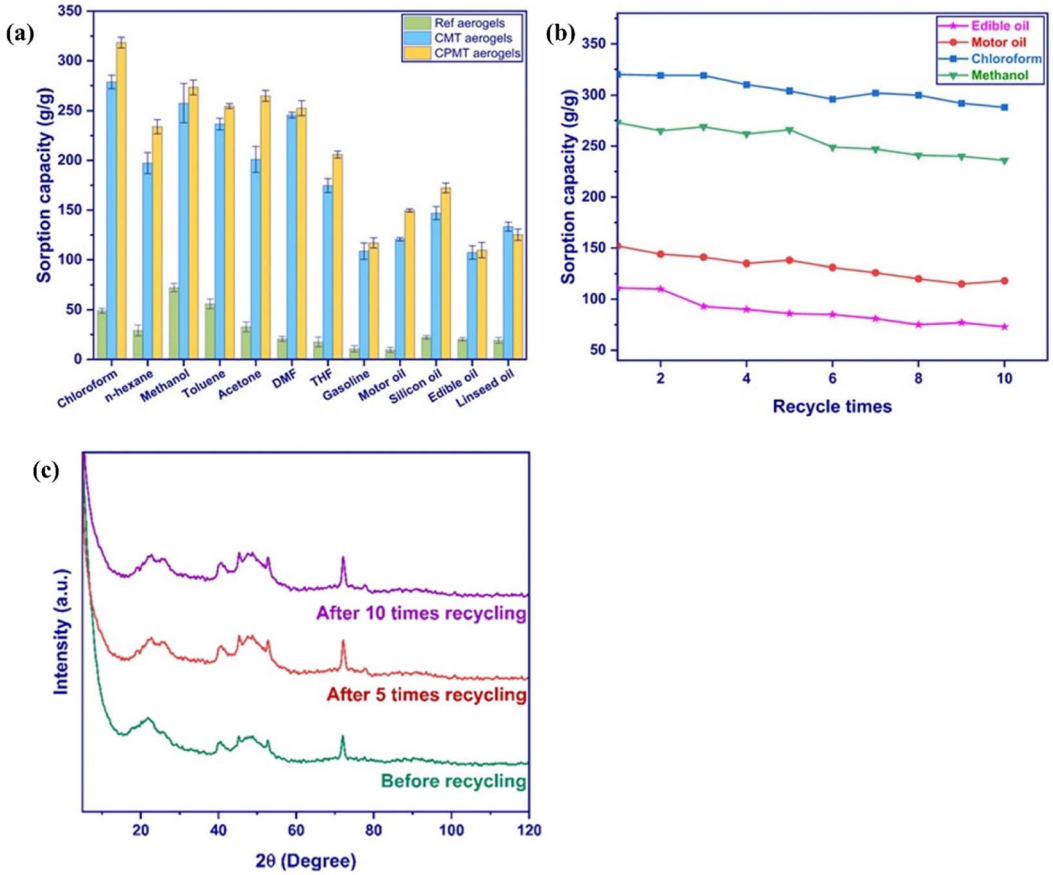

Fig. 10 (a) Sorption capacity of Ref., CMT, and CPMT cryogels for various oils and organic solvents, (b) recyclability of the CPMT cryogel after ten cycles of squeezing, and (c) XRD patterns of CPMT cryogel before and after 5 and 10 times recycling.

Reusability, recyclability, and chemical stability of cryogels is critical for their practical applications as sorbents for oils and organic solvents. Although the fluids can be recovered from saturated sorbents *via* distillation, solvent extraction, or combustion, these methods are often complicated, time-consuming, inefficient, and energy-intensive.[34] In this study, oils/organic solvents were recovered using a simple mechanical squeezing that can be considered the simplest and most sustainable recycling approach regarding energy, material, and chemical use. Fig. 10b shows the sorption capacity of recovered CPMT cryogels for motor oil, edible oil, chloroform, and methanol. The CPMT cryogel retained the high sorption capacity with all tested oils and organic solvents even after 10 cycles of squeezing–sorption, showing only a slight decrease in removal efficiency and indicating the good cryogels recyclability.

Furthermore, to confirm the reusability of the CPMT cryogels, the XRD patterns of the cryogels prior to exposure to chloroform (the highest sorption capacity) and after five and ten cycles of squeezing were measured. As shown in Fig. 10c, there is no significant difference in the patterns of the cryogels before and after dipping into chloroform, which indicates their excellent recyclability and chemical stability.

The chemical stability of the CPMT cryogels was also confirmed by exposing them to motor oil, silicon oil, chloroform, and methanol for10 min and 24 hours. Video S3 and S4† show that after removing the cryogels from the oil/organic solvents, they were still solid and rigid even after 24 h. The color of the oil/solvent remained unchanged, indicating that the CPMT cryogels are chemically stable and have a good structural integrity.

The as-prepared CPMT cryogel possessed ultrahigh sorption capacity, being one of the highest reported in the literature fabricated by only pure CNCs or CNFs cryogels or complicated and high-cost approaches (Table 3), including aerogels and sponges of chemically cross-linked cellulose aero- and cryogels (12–168 g g^{-1}),[21,34,39,77–80] MXene based aerogels and sponges,[40,46–48,81–83] carbon aerogels,[12,84–86] and graphene-based aerogels.[87,88] The sorption capacity of CPMT, especially, outperforms that of previously studied porous MXene materials. Thus, the straightforward fabrication process and abundant green resources of cellulose nanomaterials make CPMT cryogel a highly appealing, cost-effective, and sustainable alternative for water remediation.

Table 3 Comparison of the oil and organic solvent sorption capacity of different sorbents with our prepared CPMT cryogel

Sorbents	Absorbed substances	Sorption capacity ($g\ g^{-1}$)	Ref.
Modified cellulose aerogel	Crude oil, engine oil, pump oil, paraffin liquid, silicon oil. DMSO, cyclohexane, isopropyl alcohol, CH_2Cl_2	9–48	21
Silane modified cellulose/PVA aerogel	Trichloromethane, dichloromethane, chlorobenzene, hexane, cyclohexane, toluene, peanut oil	28–65	78
CNCs/PVA aerogel	Gasoline, motor oil, crude oil, sesame oil, cooking oil, and olive oil, chloroform, acetone, ethanol, DMF, 2-propanol, ethyl acetate, toluene, hexane	69–168	39
Copper nanoparticles-coated cellulose aerogel	*n*-Hexane, trichloromethane, soybean oil, pump oil	67.8–164.5	80
Polyimide/MXene aerogel	Pump oil, chloroform, tetrahydrofuran, soybean oil, acetone, toluene, *n*-hexane, waste pump oil	18–58	40
MXene functionalized melamine sponge	*n*-Hexane, soybean oil, diesel oil, silicone oil, lubricating oil, toluene, petroleum ether and cyclohexane	60–112	81
Polyimide nanofiber/MXene aerogel	*n*-hexane, ethanol, isopropanol, soybean oil, acetone, ethyl acetate, ethanediol, CCl_4	55.85–135.29	46
Polyurethane sponge wrapped with MXene	Hexane, toluene, pump oil, vegetable oil, silicone oil, ethylene glycol	20–42	82
MXene-based melamine sponge	Petroleum ether, ethyl acetate, toluene, DCM, chloroform	80–176	47
CNCs/MXene aerogel	DMSO, DMF, olive, pump oil, soybean oil, diesel oil, acetone	45–63	48
MXene/RGO/carbon hybrid aerogel	*n*-Hexane, toluene, *N*,*N*-DMF, DMSO	50–90	83
Carbon aerogel	*n*-Hexane, toluene, pump oil, soybean oil, chloroform, dichloromethane	80–161	84
Carbon aerogel	Acetone, toluene, chloroform, pump oil, soybean oil, nitrobenzene, gasoline, dichloromethane	105–276	12
Carbon nanofiber aerogel	Gasoline, diesel oil, 2-propanol, diethyl ether, methanol, toluene, palm oil, soy oil, sunflower oil, coconut oil, cyclohexane	37–87	86
Carbon nanofiber aerogels	Toluene, cyclohexane, acetone, methanol, diethyl ether, gasoline, pump oil, palm oil, soy oil, sunflower oil, coconut oil	35–85	85
Graphene aerogel	*n*-Hexane, octane, hexadecane, toluene, chloroform, diesel oil, crude oil, engine oil, peanut oil, gasoline	109–236	87
Cysteamine/L-ascorbic acid graphene aerogel	*n*-Hexane, ethanol, petroleum ether, methylbenzene, gasoline, light crude oil	Up to 310	88
CPMT cryogel–this work		110–320	

4. Conclusion

In summary, a mechanically robust hybrid, double cross-linked cryogel of NC (combination of CNCs and CNFs), PVA, TDA, and MXene with superhydrophobicity (WCA ~150°), low density (~20 mg cm^{-3}), high porosity (≥92%), and ultrahigh sorption capacity (>300 $g\ g^{-1}$) was fabricated using a simple freeze–drying process. CNCs and CNFs were prepared *via* a green DESs-

based technique, whereas MXene nanosheets $Ti_3C_2T_x$, were synthesized *via* the etching of Al layers of MAX phase (Ti_3AlC_2) and ultrasonic exfoliation. In ref. cryogels with a combination of CNCs and CNFs, the mechanical performance of the cryogels were significantly higher than those of pure CNCs or CNFs. Due to the strong interaction between NC, PVA chains, and MXene nanosheets, the CNCs–CNFs/PVA/TDA@MXene cryogels displayed mechanical durability and superior fluid sorption capacity (110–320 g g^{-1}) toward various oils and organic solvents. The sorption capacity was one of the highest reported in the literature for bio-based porous solids. The hybrid cryogels could not only selectively absorb oils and organic solvents from polluted water but also exhibited a very good recyclability rate (at least 10 cycles), suggesting their great potential in oil/water separation. Thus, the CPMT cryogel is a highly appealing, cost-effective, and sustainable material for water remediation because of its simple fabrication process and abundant green resources of cellulose nanomaterials.

Conflicts of interest

The authors declare that they have no known competing financial interests or personal relationships that could have appeared to influence the work reported in this paper.

Acknowledgements

The authors acknowledge the support from the Academy of Finland project "ACNF" (325276). The SEM part of the work was carried out with the support of the Centre for Material Analysis, University of Oulu, Finland. Also, the authors would like to express their gratitude to Ferdowsi University of Mashhad for supporting this project (Grant no. 3/52259).

References

1 E. S. Ferreira, C. A. Rezende and E. D. Cranston, *Green Chem.*, 2021, **23**, 3542–3568.
2 S. ben Hammouda, Z. Chen, C. An and K. Lee, *J. Clean. Prod.*, 2021, **311**, 127630.
3 L. Yi, Y. Xia, Z. Tan, X. Fang, L. Zhao, H. Wu and S. Guo, *J. Clean. Prod.*, 2020, **264**, 121558.
4 W. Ma, Z. Jiang, T. Lu, R. Xiong and C. Huang, *Chem. Eng. J.*, 2022, **430**, 132989.
5 E. K. Sam, J. Liu and X. Lv, *Ind. Eng. Chem. Res.*, 2021, **60**, 2353–2364.
6 Y. Lv, X. Xi, L. Dai, S. Tong and Z. Chen, *Adv. Mater. Interfac.*, 2021, **8**, 2002030.
7 R. Ganesamoorthy, V. K. Vadivel, R. Kumar, O. S. Kushwaha and H. Mamane, *J. Clean. Prod.*, 2021, **329**, 129713.
8 Z. Xue, Y. Cao, N. Liu, L. Feng and L. Jiang, *J. Mater. Chem. A*, 2014, **2**, 2445–2460.
9 W. Li, K. Liu, Y. Zhang, S. Guo, Z. Li and S. C. Tan, *Chem. Eng. J.*, 2022, **446**, 137195.
10 H. Li, P. Mu, J. Li and Q. Wang, *J. Mater. Chem. A*, 2021, **9**, 4167–4175.
11 M. Wu, G. Shi, W. Liu, Y. Long, P. Mu and J. Li, *ACS Appl. Mater. Interfaces*, 2021, **13**, 14759–14767.
12 J. Dong, J. Zeng, B. Wang, Z. Cheng, J. Xu, W. Gao and K. Chen, *ACS Appl. Mater. Interfaces*, 2021, **13**, 15910–15924.
13 P. K. Renjith, C. Sarathchandran, V. Sivanandan Achary, N. Chandramohanakumar and V. Sekkar, *J. Hazard. Mater.*, 2021, **415**, 125548.
14 Y. Fang, L. Yan and H. Liu, *ACS Appl. Polym. Mater.*, 2020, **2**, 3781–3788.
15 A. Jamsaz and E. K. Goharshadi, *J. Mol. Liq.*, 2020, **307**, 112979.
16 A. Jamsaz, E. K. Goharshadi, A. Barras, M. Ifires, S. Szunerits and R. Boukherroub, *Sep. Purif. Technol.*, 2021, **274**, 118931.
17 Z. Tajmoradi, H. Roghani-Mamaqani and M. Salami-Kalajahi, *Chem. Eng. J.*, 2021, **417**, 128005.
18 F. Wahid, X.-J. Zhao, Y.-X. Duan, X.-Q. Zhao, S.-R. Jia and C. Zhong, *Carbohydr. Polym.*, 2021, **257**, 117611.
19 R. K. Gupta, G. J. Dunderdale, M. W. England and A. Hozumi, *J. Mater. Chem. A*, 2017, **5**, 16025–16058.
20 N. Zhang, Y. Qi, Y. Zhang, J. Luo, P. Cui and W. Jiang, *Ind. Eng. Chem. Res.*, 2020, **59**, 14546–14568.
21 X. Xu, F. Dong, X. Yang, H. Liu, L. Guo, Y. Qian, A. Wang, S. Wang and J. Luo, *J. Agric. Food Chem.*, 2019, **67**, 637–643.
22 M. Rajinipriya, M. Nagalakshmaiah, M. Robert and S. Elkoun, *ACS Sustain. Chem. Eng.*, 2018, **6**, 2807–2828.
23 X. Yue, T. Zhang, D. Yang, F. Qiu and Z. Li, *J. Clean. Prod.*, 2018, **199**, 411–419.
24 G. Kumar, D. T. K. Dora, D. Jadav, A. Naudiyal, A. Singh and T. Roy, *J. Clean. Prod.*, 2021, **298**, 126744.
25 G. Akhlamadi, E. K. Goharshadi and S. V. Saghir, *Ceram. Int.*, 2021, **19**, 27042–27049.
26 Y. Ji, Y. Wen, Z. Wang, S. Zhang and M. Guo, *J. Clean. Prod.*, 2020, **255**, 120276.
27 Y. Fu and Z. Guo, *J. Mater. Chem. A*, 2022, **10**, 8129–8158.
28 Y.-D. Dong, H. Zhang, G.-J. Zhong, G. Yao and B. Lai, *Chem. Eng. J.*, 2021, **405**, 126980.
29 H. Maleki, *Chem. Eng. J.*, 2016, **300**, 98–118.
30 H. Liu, B. Geng, Y. Chen and H. Wang, *ACS Sustain. Chem. Eng.*, 2017, **5**, 49–66.
31 T. Zhang, Y. Zhang, X. Wang, S. Liu and Y. Yao, *Mater. Lett.*, 2018, **229**, 103–106.
32 R. Lin, A. Li, T. Zheng, L. Lu and Y. Cao, *RSC Adv.*, 2015, **5**, 82027–82033.
33 G. Akhlamadi and E. K. Goharshadi, *Process Saf. Environ. Prot.*, 2021, **154**, 155–167.
34 O. Laitinen, T. Suopajärvi, M. Österberg and H. Liimatainen, *ACS Appl. Mater. Interfaces*, 2017, **9**, 25029–25037.
35 M. Mu, Y. Li, H.-Y. Yu, Z. Li, Y. Cao and X. Chen, *ACS Sustain. Chem. Eng.*, 2021, **9**, 9951–9960.
36 L. Guo, Z. Chen, S. Lyu, F. Fu and S. Wang, *Carbohydr. Polym.*, 2018, **179**, 333–340.
37 D. Wang, H. Yu, X. Fan, J. Gu, S. Ye, J. Yao and Q. Ni, *ACS Appl. Mater. Interfaces*, 2018, **10**, 20755–20766.
38 L. Liang, S. Bhagia, M. Li, C. Huang and A. J. Ragauskas, *ChemSusChem*, 2020, **13**, 78–87.
39 G. Akhlamadi and E. K. Goharshadi, *Process Saf. Environ. Prot.*, 2021, **154**, 155–167.

40 N.-N. Wang, H. Wang, Y.-Y. Wang, Y.-H. Wei, J.-Y. Si, A. C. Y. Yuen, J.-S. Xie, B. Yu, S.-E. Zhu, H.-D. Lu, W. Yang, Q. N. Chan and G.-H. Yeoh, *ACS Appl. Mater. Interfaces*, 2019, **11**, 40512–40523.
41 W. Tian, A. VahidMohammadi, M. S. Reid, Z. Wang, L. Ouyang, J. Erlandsson, T. Pettersson, L. Wågberg, M. Beidaghi and M. M. Hamedi, *Adv. Mater.*, 2019, **31**, 1902977.
42 C. E. Shuck, A. Sarycheva, M. Anayee, A. Levitt, Y. Zhu, S. Uzun, V. Balitskiy, V. Zahorodna, O. Gogotsi and Y. Gogotsi, *Adv. Eng. Mater.*, 2020, **22**, 1901241.
43 K. Rasool, R. P. Pandey, P. A. Rasheed, S. Buczek, Y. Gogotsi and K. A. Mahmoud, *Mater. Today*, 2019, **30**, 80–102.
44 S. Mallakpour, V. Behranvand and C. M. Hussain, *Ceram. Int.*, 2021, **47**, 26585–26597.
45 R. Bian, G. He, W. Zhi, S. Xiang, T. Wang and D. Cai, *J. Mater. Chem. C*, 2019, **7**, 474–478.
46 H. Liu, X. Chen, Y. Zheng, D. Zhang, Y. Zhao, C. Wang, C. Pan, C. Liu and C. Shen, *Adv. Funct. Mater.*, 2021, **31**, 2008006.
47 M. Wang, J. Zhu, Y. Zi and W. Huang, *ACS Appl. Mater. Interfaces*, 2021, **13**, 47302–47312.
48 C. Cai, Z. Wei, Y. Huang and Y. Fu, *Chem. Eng. J.*, 2021, **421**, 127772.
49 X. Gong, Y. Wang, H. Zeng, M. Betti and L. Chen, *ACS Sustain. Chem. Eng.*, 2019, **7**, 11118–11128.
50 X. Zhang, H. Wang, Z. Cai, N. Yan, M. Liu and Y. Yu, *ACS Sustain. Chem. Eng.*, 2018, **7**, 332–340.
51 L. Zhou and Z. Xu, *J. Hazard. Mater.*, 2020, **388**, 121804.
52 J. A. Sirviö, M. Visanko and H. Liimatainen, *Biomacromolecules*, 2016, **17**, 3025–3032.
53 O. Laitinen, J. Ojala, J. A. Sirviö and H. Liimatainen, *Cellulose*, 2017, **24**, 1679–1689.
54 J. A. Sirviö, M. Visanko and H. Liimatainen, *Green Chem.*, 2015, **17**, 3401–3406.
55 M. Alhabeb, K. Maleski, B. Anasori, P. Lelyukh, L. Clark, S. Sin and Y. Gogotsi, *Chem. Mater.*, 2017, **29**, 7633–7644.
56 L. Ding, Y. Wei, L. Li, T. Zhang, H. Wang, J. Xue, L.-X. Ding, S. Wang, J. Caro and Y. Gogotsi, *Nat. Commun.*, 2018, **9**, 155.
57 W. Peng, R. Hu, W. Jiang, J. Kang, J. Li, Y. Cao and M. Xiang, *ACS Omega*, 2021, **6**, 19973–19982.
58 T. Zhang, W. Zhang, H. Xi, Q. Li, M. Shen, G. Ying and J. Zhang, *Cellulose*, 2021, **28**, 4281–4293.
59 M. Naguib, M. Kurtoglu, V. Presser, J. Lu, J. Niu, M. Heon, L. Hultman, Y. Gogotsi and M. W. Barsoum, *Adv. Mater.*, 2011, **23**, 4248–4253.
60 J. Hu, Y. Zhan, G. Zhang, Q. Feng, W. Yang, Y.-H. Chiao, S. Zhang and A. Sun, *J. Membr. Sci.*, 2021, **637**, 119627.
61 J. Luo, X. Tao, J. Zhang, Y. Xia, H. Huang, L. Zhang, Y. Gan, C. Liang and W. Zhang, *ACS Nano*, 2016, **10**, 2491–2499.
62 B. Rashid, A. Anwar, S. Shahabuddin, G. Mohan, R. Saidur, N. Aslfattahi and N. Sridewi, *Materials*, 2021, **14**, 4370.
63 L. Wang, H. Liu, X. Lv, G. Cui and G. Gu, *J. Alloys Compd.*, 2020, **828**, 154251.
64 W. Feng, H. Luo, Y. Wang, S. Zeng, L. Deng, X. Zhou, H. Zhang and S. Peng, *RSC Adv.*, 2018, **8**, 2398–2403.
65 A. Pazniak, P. Bazhin, N. Shplis, E. Kolesnikov, I. Shchetinin, A. Komissarov, J. Polcak, A. Stolin and D. Kuznetsov, *Mater. Des.*, 2019, **183**, 108143.
66 A. Feng, Y. Yu, Y. Wang, F. Jiang, Y. Yu, L. Mi and L. Song, *Mater. Des.*, 2017, **114**, 161–166.
67 F. Shi, J. Sun, J. Wang, M. Liu, Z. Yan, B. Zhu, Y. Li and X. Cao, *J. Membr. Sci.*, 2021, **620**, 118850.
68 Y. Cao, Q. Deng, Z. Liu, D. Shen, T. Wang, Q. Huang, S. Du, N. Jiang, C.-T. Lin and J. Yu, *RSC Adv.*, 2017, **7**, 20494–20501.
69 Y. Guo, X. Zhou, D. Wang, X. Xu and Q. Xu, *Langmuir*, 2019, **35**, 14481–14485.
70 M. Ghidiu, J. Halim, S. Kota, D. Bish, Y. Gogotsi and M. W. Barsoum, *Chem. Mater.*, 2016, **28**, 3507–3514.
71 J. Halim, K. M. Cook, M. Naguib, P. Eklund, Y. Gogotsi, J. Rosen and M. W. Barsoum, *Appl. Surf. Sci.*, 2016, **362**, 406–417.
72 J. Halim, M. R. Lukatskaya, K. M. Cook, J. Lu, C. R. Smith, L.-Å. Näslund, S. J. May, L. Hultman, Y. Gogotsi, P. Eklund and M. W. Barsoum, *Chem. Mater.*, 2014, **26**, 2374–2381.
73 J. Wang, Z. Cai, D. Lin, K. Chen, L. Zhao, F. Xie, R. Su, W. Xie, P. Liu and R. Zhu, *ACS Appl. Mater. Interfaces*, 2021, **13**, 32495–32502.
74 S. A. Shah, T. Habib, H. Gao, P. Gao, W. Sun, M. J. Green and M. Radovic, *Chem. Commun.*, 2017, **53**, 400–403.
75 Y. Lu, D. Li and F. Liu, *Materials*, 2022, **15**, 307.
76 G. G. de Lima, B. D. Ferreira, M. Matos, B. L. Pereira, M. J. D. Nugent, F. A. Hansel and W. L. E. Magalhães, *Carbohydr. Polym.*, 2020, **245**, 116612.
77 C. Shi, Y. Chen, Z. Yu, S. Li, H. Chan, S. Sun, G. Chen, M. He and J. Tian, *Sustainable Mater. Technol.*, 2021, **28**, e00277.
78 Y. Yu, X. Shi, L. Liu and J. Yao, *J. Mater. Sci.*, 2021, **56**, 2763–2776.
79 Z. Wu, H. Sun, Z. Xu, H. Chi, X. Li, S. Wang, T. Zhang and Y. Zhao, *ACS Appl. Nano Mater.*, 2021, **4**, 8979–8989.
80 Z. Li, L. Zhong, T. Zhang, F. Qiu, X. Yue and D. Yang, *ACS Sustain. Chem. Eng.*, 2019, **7**, 9984–9994.
81 J. Xue, L. Zhu, X. Zhu, H. Li, C. Ma, S. Yu, D. Sun, F. Xia and Q. Xue, *Sep. Purif. Technol.*, 2021, **259**, 118106.
82 C. Gong, J. Lao, B. Wang, X. Li, G. Li, J. Gao, Y. Wan, X. Sun, R. Guo and J. Luo, *J. Mater. Chem. A*, 2020, **8**, 20162–20167.
83 D. Jiang, J. Zhang, S. Qin, D. Hegh, K. A. S. Usman, J. Wang, W. Lei, J. Liu and J. M. Razal, *ACS Appl. Mater. Interfaces*, 2021, **13**, 51333–51342.
84 L. Li, T. Hu, H. Sun, J. Zhang and A. Wang, *ACS Appl. Mater. Interfaces*, 2017, **9**, 18001–18007.
85 P. Ieamviteevanich, W. Mongkolthanaruk, K. Faungnawakij, E. Daneshvar, A. Bhatnagar and S. Pinitsoontorn, *ACS Appl. Nano Mater.*, 2022, **5**, 2885–2896.
86 P. Ieamviteevanich, D. Palaporn, N. Chanlek, Y. Poo-arporn, W. Mongkolthanaruk, S. J. Eichhorn and S. Pinitsoontorn, *ACS Appl. Nano Mater.*, 2020, **3**, 3939–3950.
87 S. Yang, C. Shen, L. Chen, C. Wang, M. Rana and P. Lv, *ACS Appl. Nano Mater.*, 2018, **1**, 531–540.
88 C. Dai, W. Sun, Z. Xu, J. Liu, J. Chen, Z. Zhu, L. Li and H. Zeng, *Langmuir*, 2020, **36**, 13698–13707.

